Subthermocline Eddies in the Kuroshio Extension Region Observed by Mooring Arrays

RUICHEN ZHU,[a,b] ZHAOHUI CHEN,[a,b] ZHIWEI ZHANG,[a,b] HAIYUAN YANG,[a,b] AND LIXIN WU[a,b]

[a] *Key Laboratory of Physical Oceanography/Institute for Advanced Ocean Science/Frontiers Science Center for Deep Ocean Multispheres and Earth System, Ocean University of China, Qingdao, China*
[b] *Pilot National Laboratory for Marine Science and Technology (Qingdao), Qingdao, China*

(Manuscript received 2 March 2020, in final form 11 November 2020)

ABSTRACT: Subthermocline eddies (STEs), also termed intrathermocline eddies or submesoscale coherent vortices, are lens-shaped eddies with anomalous water properties located in or below the thermocline. Although STEs have been discovered in many parts of the World Ocean, most of them were observed accidentally in hydrographic profiles, and direct velocity measurements are very rare. In this study, dynamic features of STEs in the Kuroshio Extension (KE) region are examined in detail using concurrent temperature/salinity and velocity measurements from mooring arrays. During the moored observation periods of 2004–06 and 2015–19, 11 single-core STEs, including 8 with warm/salty cores and 3 with cold/fresh cores, were captured. The thermohaline properties in their cores suggest that these STEs may originate from the subarctic front and the upstream Kuroshio south of Japan. The estimated radius of these STEs varied from 8 to 66 km with the mean value of ~30 km. The warm/salty STEs seemed to be larger and rotate faster than the cold/fresh ones. In addition to single-core STEs, a dual-core STE was observed in the KE recirculation region, which showed that the upper cold/fresh cores stacked vertically over the lower warm/salty cores. Based on the observed parameters of the STEs, their Rossby number and Burger number were further estimated, with values up to 0.5 and 1, respectively. Furthermore, a low Richardson number O (0.25) was found at the periphery of these STEs, suggesting that shear instability-induced turbulent mixing may be an erosion route for the STEs.

KEYWORDS: North Pacific Ocean; Eddies; In situ oceanic observations

1. Introduction

Subthermocline eddies (STEs), usually characterized by lens-like structures with nearly homogenous temperatures and salinities in or below the thermocline, are capable of transporting anomalous water properties far from the formation regions (Shapiro et al. 1995; Testor and Gascard 2003; Bower et al. 2013; L'Hégaret et al. 2014). These eddies are also termed intrathermocline eddies (Dugan et al. 1982) or submesoscale coherent vortices (SCVs; McWilliams 1985) because of their small horizontal scales and long lifespans reaching months to years (Armi et al. 1989). Generally, the lens-like STEs rotate anticyclonically and have a weak stratification minimum at the center, and they can retain their water properties for a long distance. The combination of their anticyclonic vorticity and weak stratification results in the low values of potential vorticity (PV) within their cores. Except for a few STEs that could induce sea level anomalies (e.g., Lofoten basin vortices; Yu et al. 2017; Fer et al. 2018; Bosse et al. 2019), most of them are difficult to detect by remote sensing due to their small size and weak signals at the sea surface. In most cases, they are discovered accidentally through hydrological surveys (e.g., Oka et al. 2009; Rossby et al. 2011), SOFAR or RAFOS floats (e.g., Testor and Gascard 2006; Bower et al. 2013), Argo or ice-tethered profiling floats (e.g., Timmermans et al. 2008; Zhang et al. 2015; Li et al. 2017), gliders (e.g., Bosse et al. 2015; Thomsen et al. 2016; Steinberg et al. 2019), and mooring lines (e.g., Lilly and Rhines 2002; Zhao and Timmermans 2015; Zhang et al. 2019). For regions where STEs are frequently detected, multiplatform observation is the most efficient way to investigate the entire life cycle (Armi et al. 1989; Hebert et al. 1990).

STEs have been reported in many parts of the global ocean (McWilliams 1985, 2016; Kostianoy and Belkin 1989). They are generally named based on their formation regions and water mass characteristics, for example, the Mediterranean Water eddies (Meddies) in the North Atlantic (McDowell and Rossby 1978), the California Undercurrent eddies (Cuddies) in the northeastern Pacific (Garfield et al. 1999), the KE region intermediate-layer eddies (Kiddies) in the subtropical North Pacific (Li et al. 2017), the eddies associated with Red Sea outflow (Reddies) in the Indian Ocean (Shapiro and Meschanov 1991), and other STEs east of Australia, in the Gulf of Mexico and in the eastern subtropical South Pacific Ocean (Johnson and McTaggart 2010; Baird and Ridgway 2012; Meunier et al. 2018). STEs are suggested to play important roles in transporting subsurface water masses (e.g., Pelland et al. 2013; Li et al. 2017) as well as enhancing the thermocline diapycnal mixing through shear instability (Zhang et al. 2019).

The KE in the North Pacific, where the Kuroshio leaves the western boundary and flows eastward as a free jet, has long been recognized as the key to multiscale oceanic processes and air–sea interactions (Mizuno and White 1983; Yasuda et al. 1992; Nakamura et al. 2002; Qiu and Chen 2005; Ma et al. 2015). STEs have been reported in this area in several studies. Although the earliest case report of an STE in the KE region can be traced back to the 1990s (Maximenko and Yamagata 1995), STEs have

Supplemental information related to this paper is available at the Journals Online website: https://doi.org/10.1175/JPO-D-20-0047.s1.

Corresponding author: Zhaohui Chen, chenzhaohui@ouc.edu.cn

DOI: 10.1175/JPO-D-20-0047.1

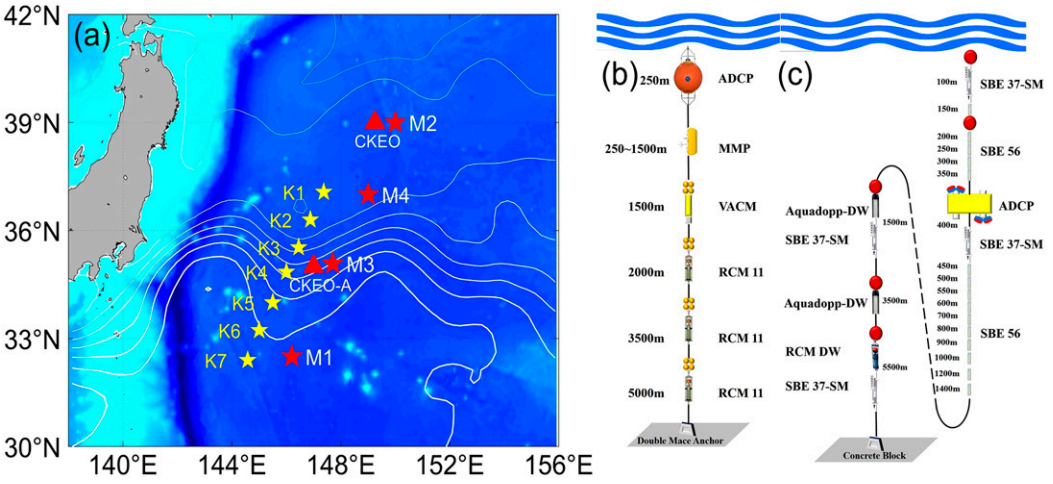

FIG. 1. (a) Locations of KESS subsurface moorings (yellow stars) from June 2004 to June 2006 and China subsurface moorings (red stars) and buoys (red triangles) from November 2015 to September 2019. The STEs recorded by K4–K7 and M1 are analyzed in this study. Contours are the long-term mean sea surface height (SSH) between 2004 and 2018. Schematic of the design of the (b) KESS moorings and (c) M1 mooring.

received much less attention than the surface-intensified mesoscale eddies. Recently, more high-resolution hydrographic transects and autonomous platforms such as Argo profiling floats and gliders are becoming available, providing new ways to study STEs systematically. For example, based on a high-resolution hydrographic survey, Oka et al. (2009) observed an STE with anomalously low PV and high dissolved oxygen south of the KE in the fall of 2008. The observed properties of this eddy are similar to those of the North Pacific Central Mode Water (CMW). In the spring of 2014, two STEs with different features of temperature, salinity and dissolved oxygen were observed by rapid-sampling Argo floats in the same area (Zhang et al. 2015). A subsequent in-depth study based on 14-yr Argo float data statistically investigated general features of STEs, with a special focus on the cold-core STEs (Li et al. 2017). The results suggested that the cold-core STEs in this region originate from the subarctic front (SAF) through subduction possibly induced by mixed layer frontogenesis (Spall 1995). Given their geographic distributions and residence depths, these STEs are named KE region intermediate-layer eddies (Kiddies for short; Li et al. 2017). Li et al. (2017) also identified many warm- and salty-core STEs in the northwestern Pacific, but their origins and associated generation processes were not conclusively addressed.

Although Argo floats and intensive shipboard hydrographic surveys have improved our understanding of the characteristics of STEs in the KE region, there remain data gaps regarding their velocity structures due to a lack of direct current velocity measurements. This data shortage is an obstacle to further understanding the dynamic features of STEs. Hence, we extend our focus to the velocity structure of STEs using subsurface moorings deployed during the Kuroshio Extension System Study (KESS) project (Donohue et al. 2008), as well as a newly designed subsurface mooring deployed and maintained by Ocean University of China, to deepen our understanding of STEs. In addition to thermodynamic properties, we report the direct velocity measurement of cold-core and warm-core STEs. The two types of STEs identified in this study show evident disparities in their sizes, water mass properties and velocity patterns, suggesting that they may originate from different places through different generation mechanisms. In addition, a subsurface dual-core STE with two vertically aligned temperature/salinity cores is reported here, apparently for the first time in the KE region. The rest of this paper is organized as follows. In section 2, we introduce the data collected by subsurface moorings and the procedure used to identify STEs and estimate their radius. In section 3, the features of STEs observed by subsurface moorings are examined. In section 4, some dynamic characteristics of STEs are presented. The possible origin and erosion of the STEs are discussed in section 5. The summary of this study is given in section 6.

2. Data and method

a. *KESS subsurface mooring data (2004–06)*

The overall goal of KESS was to identify and quantify the dynamic and thermodynamic processes governing the variability and the interaction between the Kuroshio Extension and the recirculation gyre (the website https://uskess.whoi.edu/ offers a comprehensive program description). The KESS array included inverted echo sounders with bottom pressure gauges and current meters (C-PIES), subsurface moorings, Kuroshio Extension Observatory (KEO) surface buoy and dozens of Argo profiling floats. The subsurface mooring array, as one important part of KESS, was designed to measure the time-varying density and velocity fields with a 4D mesoscale resolution, which was required to determine dynamic balances and cross-frontal exchanges of heat, salt, momentum, and PV. Seven subsurface moorings, deployed along a line crossing the axis of the KE and extending south into the southern recirculation gyre, were maintained from June 2004 to June 2006 (Fig. 1a).

The subsurface moorings were equipped with three deep Aanderaa RCM-11 acoustic current meters at 2000, 3500,

TABLE 1. Details of the instrument configuration for the M1 mooring.

Instrument	Type	Quantities	Sampling interval	Nominal depth
ADCP	Workhorse Long Ranger ADCP	2	1 h	400 m (Nov 2015–Oct 2017) 500 m (Oct 2017–May 2018) 400 m (May 2018–Sep 2019)
CM	Aquadopp-DW/Seaguard-RCM DW	3	30 min	1500 m (Nov 2015–Apr 2016) 1500 m/3500 m/5500 m (Apr 2016–Sep 2019)
CTD	SBE 37-SM MicroCAT *C*-*T* (*P*) recorder	4	5 min	400 m/800 m/2500 m/3500 m/4500 m (Nov 2015–Apr 2016) 100 m/400 m/1500 m/5500 m (Apr 2016–Sep 2019)
T chain	SBE 56 temperature logger	15	1 min	150–1400 m (Apr 2016–Oct 2017) 150–1000 m (Oct 2017–May 2018) 150–1400 m (May 2018–Sep 2019)

and 5000 m and a McLean Moored Profiler (MMP) equipped with a three-axis acoustic current meter and conductivity–temperature–depth (CTD) sensor moving between 250 and 1500 m vertically every 15 h. In addition, at approximately 250-m depth of each mooring, an upward-looking acoustic Doppler current profiler (ADCP) with a sampling interval of one hour was mounted to measure the near-surface velocity field (Fig. 1b). Two-year time series of high temporal resolution temperature, salinity and current data were obtained. However, due to the influences of strong currents, only 55% of the data from the MMPs were retrieved and corrected. It should be noted that the amplitude of velocity is multiplied by a factor of 4/3 through a comparison with the other instruments directly above or below the MMPs (Rainville et al. 2009). In this sense, we primarily use these data to discuss the qualitative characteristics of the velocity pattern rather than the precise magnitude.

b. *M1 mooring data (2015–19)*

Since 2014, China has designed and maintained the Kuroshio Extension Mooring System (KEMS) with an array of real-time subsurface moorings and surface buoys between the two crests of KE meanders, located to the east of the KESS subsurface mooring array. Following the last cruise in November 2019, there are now four subsurface moorings (M1, M2, M3, and M4) and two surface buoys (CKEO and CKEO-A) on site (Fig. 1a). In November 2015, the first subsurface mooring of KEMS (M1) was deployed at a water depth of ~5600 m south of the KE jet at 32.4°N, 146.2°E. M1 was equipped with two 75-kHz WorkHorse ADCPs, four SeaBird 37-SM CTDs, three Aquadopp-DW/Seaguard-RCM current meters, and a chain of SeaBird56 temperature loggers (see Fig. 1c and Table 1 for details). Each year, a new M1 with instruments of the same specifications replaced the old one. Until the last recovery, M1 had been maintained for almost four years and provided intensive in situ temperature/practical salinity (*T*/*S*) and current data in the upper 1500 m of ocean.

Here, we focus on the time series recorded by ADCPs and CTDs above 1500 m depth because temperature loggers did not provide salinity/pressure information and no STE was detected by other instruments below 1500 m. Specifically, the top two CTDs were mounted at 100 and 400 m with a sampling interval of 5 min. Two ADCPs were mounted at approximately 400 m, with one looking upward and the other downward. The ADCPs can roughly cover the upper 1000 m, and their sampling interval and vertical bin size were set to 1 h and 16 m, respectively. Unfortunately, between April 2016 and May 2018, the downward-looking ADCP was damaged, and the lower 500-m velocity profiles were lost during this period. Furthermore, the surface-intensified eddies or KE jet that passed through the M1 pushed the upper part of the mooring system downward, with most instruments mounted on M1 declining and tilting accordingly. The top two CTDs and two ADCPs exhibited a depth change of hundreds of meters for several weeks, and pitch/roll angles of ADCPs could reach 25° during the extreme knockdown events (marked by colored lines on the top of Fig. 2), which resulted in 15% data gap in the upper 1000-m velocities. Although the surface flow information was missing, the subsurface currents were continuously recorded (Fig. 2).

In this study region, the local inertial period is ~22 h, and the semidiurnal and diurnal tides have a typical velocity magnitude of 6 cm s^{-1}. All the data were therefore filtered by a fourth-order Butterworth low-pass filter with a cutoff frequency of 0.5 cpd (period of 2 days) to remove high-frequency motions such as tides and inertial gravity waves. The daily averaged data after quality control and low-pass filtering are used in the following analyses.

c. *Other datasets*

In addition to subsurface moorings, data from Argo floats (Argo 2000) in the domain of 25°–45°N, 135°–165°E, from June 2004 to June 2018 were used to augment the characterization of STEs. After removing the Argo floats with low-quality salinity data, a total of 884 floats were finally used in the following analysis. Besides, the *World Ocean Atlas* (*WOA13*) climatology of temperature and salinity (Locarnini et al. 2013; Zweng et al. 2013) were also used as the background field to identify candidate STEs.

The gridded daily sea surface height (SSH) and absolute surface geostrophic velocity with a spatial resolution of 1/4° from the delayed-time, merged, global ocean gridded absolute surface dynamic topography are used along with the absolute geostrophic velocities produced by the Data Unification and Altimeter Combination System (DUACS) and distributed by Archiving, Validation, and Interpretation of Satellite Data in Oceanography (AVISO) (https://www.aviso.altimetry.fr/). The altimetry data aid in excluding the "false" STEs that resemble surface-intensified eddy signals in the following subsection.

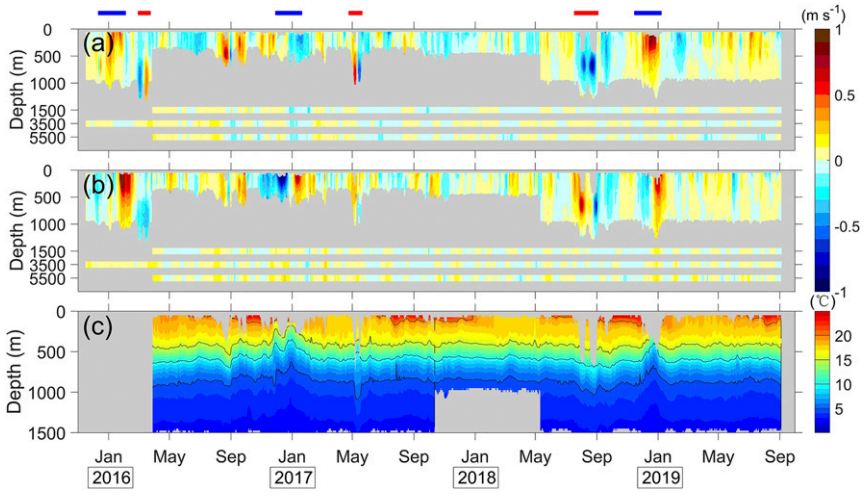

FIG. 2. Depth–time plot of (a) zonal velocity, (b) meridional velocity, and (c) temperature after 2-day smoothing from November 2015 to September 2019 by M1. Velocities measured by current meters at 1500, 3500, and 5500 m are denoted as colored line segments. Black lines in (c) are isotherms of 15°, 10°, and 5°C. The periods when surface (subthermocline) eddies cross M1 are indicated by blue (red) lines on the top of the figure. Note that there are no data for the damaged downward-looking ADCP between April 2016 and May 2018.

d. Identifying STEs

Considering the significant difference in T/S and PV between STEs and the surrounding waters, the potential temperature/salinity anomaly (T_a/S_a) and low PV are used to identify the candidate STEs. All temperature data were converted into potential temperature θ, and the θ/S values were then interpolated onto isopycnals from $25.0\sigma_0$ to $27.5\sigma_0$ with an interval of $0.05\sigma_0$. The T_a/S_a values were calculated by subtracting the mean θ/S from each profile. We used two approaches to obtaining the mean θ/S profile following Li et al. (2017): 1) from the *WOA13* climatological θ/S profiles spatially interpolated into the corresponding location of mooring or Argo floats; 2) from averaging the nearby θ/S profiles 5 days (10 days) before and after the STE event for mooring (a single Argo float).

Assuming that lateral density gradients are weak, the Ertel PV can be written as follows (Ertel 1942):

$$\mathrm{PV} = \omega_a \frac{N^2}{g} \approx \frac{f}{\rho_0}\frac{\partial \sigma_0}{\partial z}, \tag{1}$$

where ω_a is the absolute vorticity, N is the buoyancy frequency, g is the gravitational acceleration, f is the Coriolis parameter, $\rho_0 = 1030\,\mathrm{kg\,m^{-3}}$ is the reference seawater density, and σ_0 is the potential density relative to the sea surface. Although KESS and M1 moorings provided velocity profiles, the propagation speed and path of an STE was unknown at the detection stage. The relative vorticity was neglected due to the lack of the horizontal gradient of STE velocities. However, the anticyclonic vorticity of an STE can have a comparable magnitude of f and may lead to the overestimation of PV. The PV anomalies are also calculated by subtracting the mean PV from each profile, as the same to the above procedure for T_a/S_a computation.

Following the recent work by Li et al. (2017), the criteria listed below were used to identify the STEs based on moored data in the KE region:

1) local minimum or maximum S is between $\sigma_0 = 25.9$ and $27.1\,\mathrm{kg\,m^{-3}}$ with an anomaly S_a exceeding 0.15 psu;
2) the depth of the S_a maximum is below the mixed layer;
3) the thickness of S_a continuously exceeds 150 m; and
4) low PV is centered within the depth range of S_a.

After identifying all candidate STEs using the above criteria, it is helpful to double-check the SSH fields because the anomalous properties in the candidate STEs can result from advection by surface-intensified mesoscale eddies or from shifts in the KE jet. Therefore, a visual inspection was performed to ensure that there were no concurrent surface-intensified mesoscale eddies and/or KE jet within 100 km of each candidate STE; otherwise, the candidate STEs and associated T/S profiles were not taken into consideration.

e. Estimating the radius of STEs

The precise estimation of eddy radius is a prerequisite to investigating the dynamic features of STEs. Here, the moored current velocity measurements were used to estimate the radius of STEs. For each mooring-observed STE event (see section 2d), its corresponding velocity fields generally exhibit an eddy pattern with two maxima in the time series. The elapsed time T_e and thickness H of an STE are determined using the velocity contour with a magnitude of 0.3 times the velocity maxima. This criterion was used because it can completely extract the STE signals from the background flow. Then, we selected a key section of the velocity field $\mathbf{V}$ within H during the period from $T_e - 5$ to $T_e + 5$ days (as shown in Figs. 3a,b).

According to Lilly and Rhines (2002) and De Jong et al. (2014), the Rankine eddy is a good model with which to depict

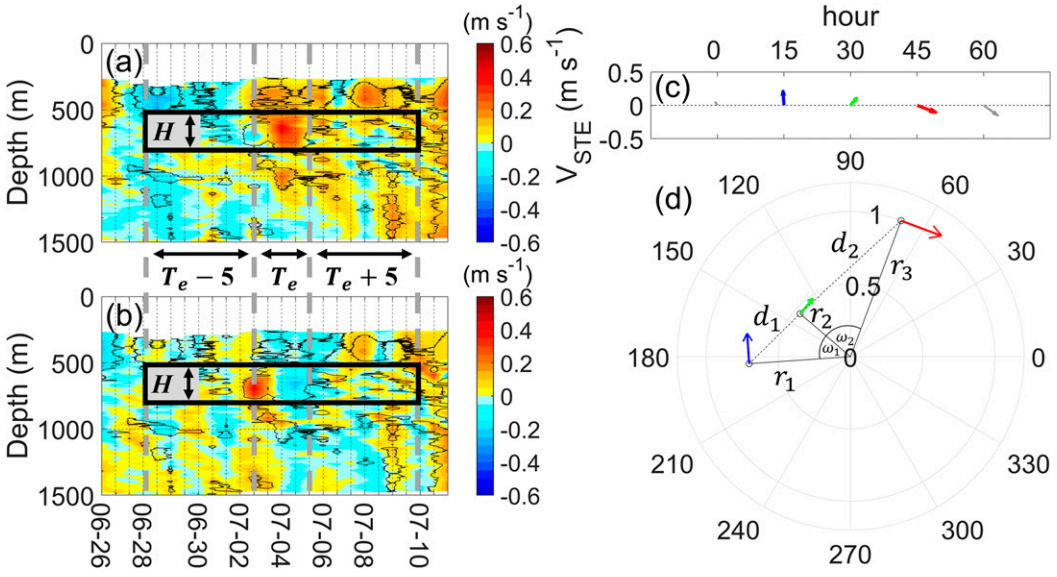

FIG. 3. Depth–time plot of (a) zonal velocity and (b) meridional velocity from K6. The black rectangle is the key section **V** with the elapsed time T_e and the thickness H, according to the peak total velocity times 0.3 (black contour). (c) The swirl velocity vectors $\mathbf{V}_{\mathrm{STE}}$. The blue and red vectors are the two maxima, as in (d). The dots in (d) are mooring positions relative to the STE center. The gray dashed line is the possible path from the blue vector to the red vector.

the velocity structure of ocean eddies. This eddy model has a core in a solid body rotation, and its azimuthal velocity is defined as follows:

$$\begin{aligned} v_\theta(r) &= V_{\max}\frac{r}{R}, \quad r \le R \\ v_\theta(r) &= V_{\max}\frac{R}{r}, \quad R < r, \end{aligned} \tag{2}$$

where r is the distance to the eddy core and R is the eddy radius with maximum azimuthal velocity $V_{\max}$. The entire radial component of velocity is zero so that the velocity vector at any point is perpendicular to the radius of that point. In this way, we can mark the position of each velocity vector in the eddy model using the time series of the swirl velocity of STEs $\mathbf{V}_{\mathrm{STE}}$ (Fig. 3d). Here, the $\mathbf{V}_{\mathrm{STE}}$ was obtained by subtracting the background velocity $\mathbf{V}_b$ from the original velocity **V**. The $\mathbf{V}_b$ was estimated by averaging **V** between $T_e - 5$ and $T_e + 5$ at each depth. Note that each position in the eddy model was also the distance between the mooring and the eddy center at that moment. The possible path by which the STE crossed the mooring, therefore, can be deduced by linking these positions in chronological order.

Next, we use two adjacent positions, r_i and r_{i+1} from the eddy center, based on the above path to calculate R (Fig. 3d). Given that the horizontal scales of STEs or SCVs are smaller than the first baroclinic Rossby deformation radius, their propagations are primarily caused by the background flow advection (McWilliams 1985). Assuming that an STE was advected through the mooring by background flow, the distance (d_i) between the two adjacent positions can be approximately derived by $|\mathbf{V}_b|$ times the time interval (t; i.e., 15 h for KESS mooring and one day for M1 in this case). With the angle ω_i between r_i and r_{i+1}, R can be yielded by the law of cosine:

$$\begin{aligned} \hat{R}_i &= \sqrt{\frac{d_i^2}{r_i^2 + r_{i+1}^2 - 2r_i r_{i+1}\cos(\omega_i)}} \\ &= \sqrt{\frac{(\mathbf{V}_b t)^2}{\dfrac{v_\theta^2(r_i)}{V_{\max}^2} + \dfrac{v_\theta^2(r_{i+1})}{V_{\max}^2} - 2\dfrac{v_\theta(r_i)v_{\theta+1}(r_{i+1})}{V_{\max}^2}\cos(\omega_i)}}, \\ i &= 1, 2, \ldots, k-1, \end{aligned} \tag{3}$$

where k is the number of positions on this path. We can obtain $k - 1$ estimates for R by using all positions. For the case in which $k > 2$, the arithmetic mean was considered as the final radius R, and the standard deviation of these estimates was defined as the uncertainty.

3. Observed features of STEs

In this section, we report direct observations from KESS and M1 moorings to present the velocity pattern and the θ/S properties of STEs. Based on the STE identification procedure described in section 2d, nine single-core STEs were detected using KESS moorings during the 2-yr observation period, including three cold-core STEs (C1, C2, and C3) in K5 and K6 in 2004 and six warm-core STEs (W1–W6) in K4, K5, K6, and K7 from December 2004 to January 2006. Two warm-core STEs (W7 and W8) were captured by the M1 mooring in March 2016 and August 2018. In addition, a dual-core STE (D1) was captured by M1 in May 2017. Other moorings (K1, K2, K3, M2, and M3) located near the KE axis or farther north did not capture any STEs.

a. STEs observed by KESS moorings

Figure 4 shows the time–depth plots of T/S and velocity for a cold-core STE (C1) captured by the mooring K6 in July 2004.

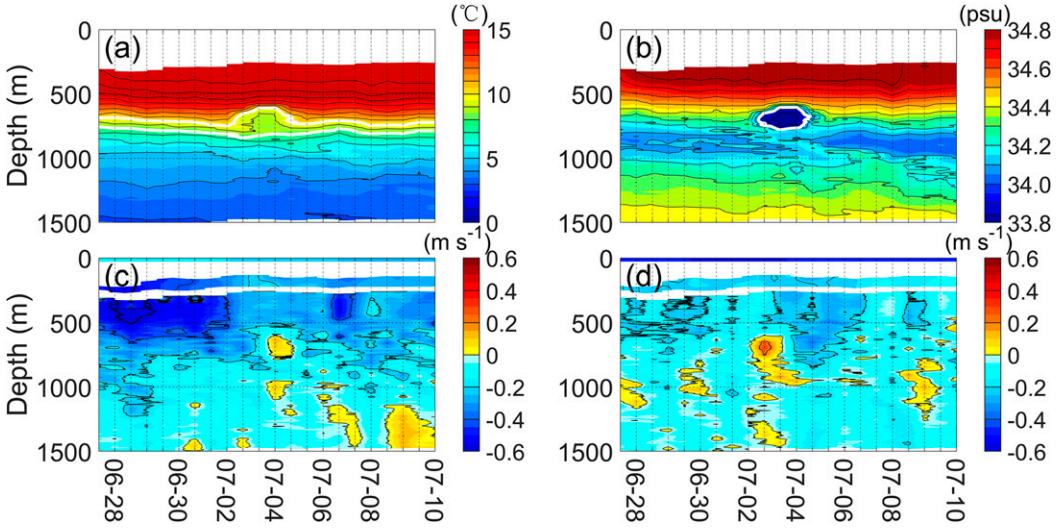

FIG. 4. Depth–time plot of (a) in-site temperature T, (b) salinity S, (c) zonal velocity U, and (d) meridional velocity V containing a cold-core STE (C1) from K6. The contour intervals for T, S, U, and V are 1°C, 0.1 psu, and 0.2 m s^{-1}, respectively. The thick white lines in (a) and (b) denote isolines of 8°C, 10°C, and 34.0 psu. The velocities in (c) and (d) are the surface geostrophic currents derived from the altimetry data.

A homogenous lens-like structure with cold and freshwater was found between 520 and 800 m from 2 to 5 July (Figs. 4a,b). Corresponding to the T/S anomalies, a concomitant STE velocity pattern can be seen from the depth–time distribution of velocity (Figs. 4c,d). At the lens periphery, $V_{\max}$ is 0.47 m s^{-1}, which is larger than the background velocity magnitude ($|\mathbf{V}_b| = 0.31$ m s^{-1}). In particular, the meridional component of velocity reverses direction as the center of the lens crosses the mooring, while no similar signals can be seen at the sea surface. Based on the above phenomena, this lens-like structure is indicative of a typical cold-core STE.

Figures 5a and 5b show the T_a and S_a calculated on the isopycnals, respectively. The results indicate that high T_a and S_a values mainly occur between 26.1σ_0 and 26.4σ_0, with highest values up to −2.63°C and −0.57 psu, respectively, at ~26.3σ_0 (Figs. 5a–c). The θ/S contrast between the STE and surrounding

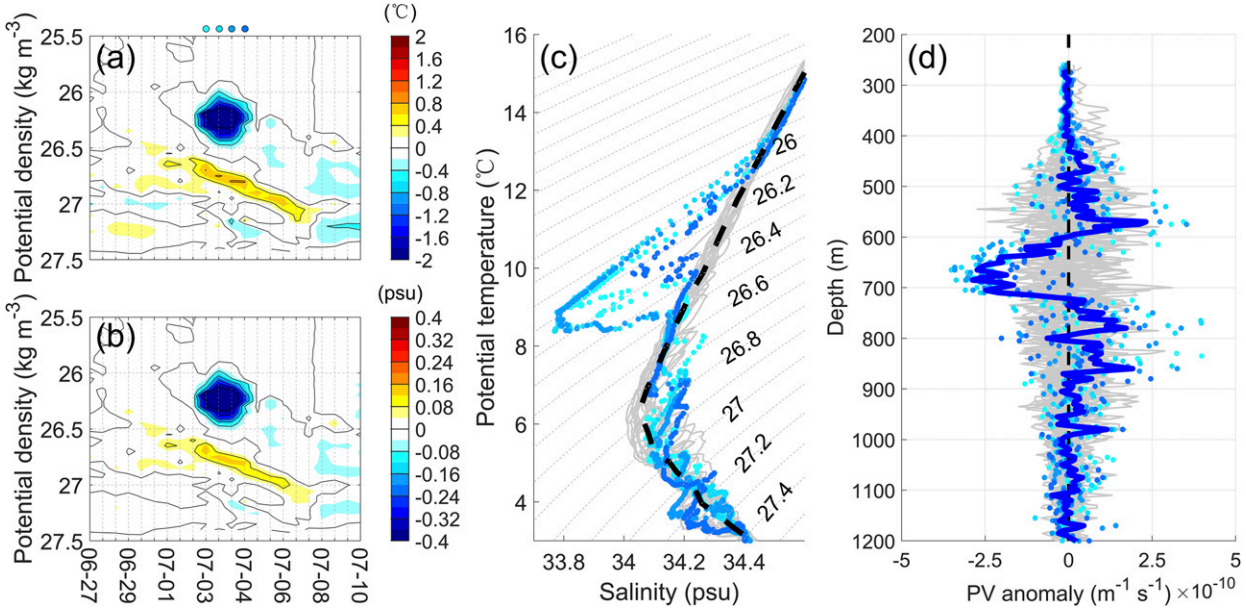

FIG. 5. Depth–time plot of (a) T_a and (b) S_a anomalies on sigma levels from the θ/S measurement by K6. (c) The θ–S diagram. The black dashed line is derived from the *WOA13* data in July, and the gray lines are from the θ/S measurements from K6 during the non-STE event. (d) PV anomalies as a function of depth. The blue dots denote the profiles derived from each θ/S measurement from K6 during the STE (C1) passage [blue dots in (a) for reference time]. The dark blue line shows the average.

TABLE 2. STEs observed by KESS and M1 moorings. Here, T_e is the elapsed time; T_a/S_a is the potential temperature/practical salinity anomaly within the STE core; H is the thickness; R is the radius estimate; V_{max} is the maximum swirl velocity; $\mathbf{V}_b$ is the magnitude and direction of background flow; N^2 is the squared buoyancy frequency averaged over H within the STE; PV_a is the potential vorticity anomaly; Ro is the Rossby number; and Bu is the Burger number.

Mooring	ID	Date	T_e (h)	T_a (°C)	S_a (psu)	H (m)	R (km)	V_{max} (m s^{-1})	$\mathbf{V}_b$ (m s^{-1})	N^2 (s^{-2}) ($\times10^{-6}$)	PV_a (m^{-1} s^{-1}) ($\times10^{-6}$)	Ro	Bu
K6	C1	Jul 2004	90	−2.63	−0.57	280	26.5 ± 11.8	0.47	0.31 (−155°)	0.34	−2.94	0.45	0.45
K5	C2	Aug 2004	45	−2.53	−0.55	180	20.3	0.33	0.40 (−43°)	1.10	−2.72	0.41	0.32
K5	C3	Sep 2004	60	−2.17	−0.48	220	17.3	0.43	0.40 (−83°)	13.0	−1.71	0.63	0.66
K5	W1	Dec 2004	135	+1.18	+0.21	500	38.9 ± 22.8	0.64	0.23 (−78°)	3.83	−1.93	0.42	0.67
K6	W2	Aug 2004	45	+0.35	+0.07	170	8.3	0.29	0.27 (−168°)	12.4	−1.78	0.89	1.71
K4	W3	Jun 2005	165	+0.92	+0.14	820	34.0 ± 15.5	0.67	0.22 (−56°)	3.70	−1.78	0.50	2.37
K5	W4	Oct 2005	225	+0.46	+0.10	520	66.9 ± 26.6	0.85	0.29 (−71°)	3.24	−1.96	0.32	0.25
K6	W5	Jan 2006	210	+0.92	+0.15	690	15.5 ± 12.3	0.70	0.06 (−16°)	1.06	−2.37	1.15	8.07
K7	W6	Jan 2006	240	+1.24	+0.21	680	44.1 ± 25.7	0.88	0.19 (−137°)	8.61	−1.87	0.51	0.97
M1	W7	Mar 2016	258	+0.82	+0.13	>600	35.9 ± 18.0	0.55	0.08 (−119°)	1.42	−1.26	0.39	1.14
M1	W8	Aug 2018	555	+0.67	+0.15	>600	30.7 ± 19.0	0.89	0.03 (−67°)	3.04	−1.84	0.74	1.56
M1	D1	May 2017	96	−1.31 +1.18	−0.31 +0.19	100 >500	38.3 ± 28.6	0.64	0.08 (−90°)	6.77 3.25	−2.63 −1.48	0.43	1.00

waters is greater than the results reported in Zhang et al. (2015), who discovered a cold-core STE with a maximum T_a/S_a of −1.95°C/−0.34 psu. The homogeneity of the θ/S properties of the STE is reflected in a relatively low PV between 600 and 720 m (Fig. 5d). The other two cold-core STEs (i.e., C2 and C3) share similar features with C1, and the details are shown in Table 2 and Figs. S1 and S2 in the online supplemental material.

In addition to cold-core STEs, the KESS mooring array also captured six warm-core STEs. Here, we take the warm-core STE (W1) captured by K5 in December 2004 as an example to show the features of these STEs. STE W1 was located between 560 and 1060 m, and it took ~5 days to cross the mooring (Figs. 6a,b). The H and T_e values were higher than those in the cold-core STEs, which may indicate a larger horizontal scale for the warm-core STEs. The eddy pattern can be clearly seen from the depth-time variation of velocity, which was first southwestward and then shifted to northeastward (Figs. 6c,d). The V_{max} of STE W1 was as large as 0.64 m s^{-1} (Fig. 6c). The anomalous water mass of W1 was located between 26.4σ_0 and 26.7σ_0 (Figs. 7a,b), and the largest T_a and S_a reached +1.18°C and +0.21 psu at 26.7σ_0, respectively (Fig. 7c), which are similar to the warm/salty STE reported by Zhang et al. (2015). The other five warm-core STEs (W2–W6) have the similar features as W1, and the details can be found in Table 2 and Figs. S3–S7.

b. *General features of current and temperature observed by M1*

Similar to the KESS moorings, the STEs were also captured by the mooring M1. South of the KE axis, the currents are

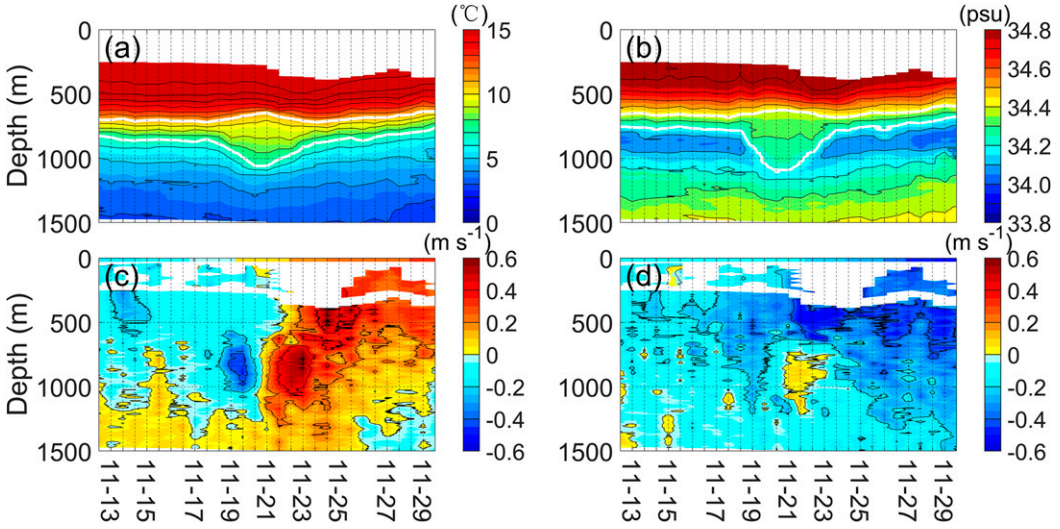

FIG. 6. As in Fig. 4, but for a warm-core STE (W1) from K5. The thick white lines in (a) and (b) are isolines of 7°C, 11°C, 34.2 psu, and 34.4 psu, respectively.

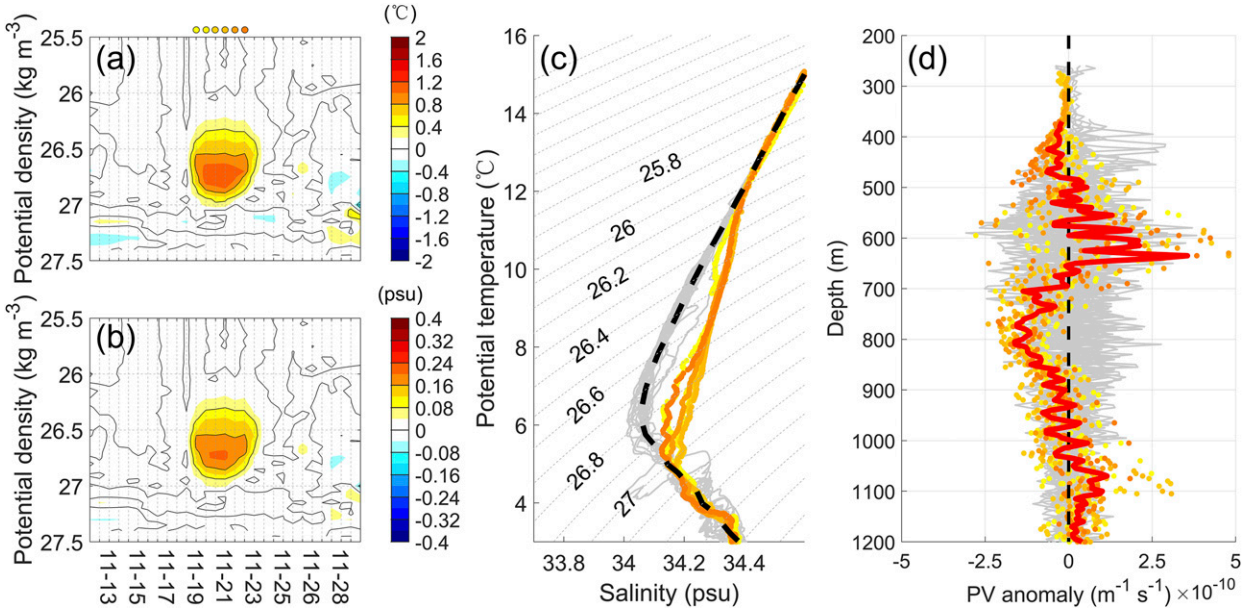

FIG. 7. As in Fig. 5, but for a warm-core STE (W1) from K5.

largely modulated by mesoscale rings shed by the Kuroshio meanders. During the observation period, three cyclonic mesoscale rings passed M1 in 2016, 2017, and 2018 (Fig. 2). Due to the strong currents associated with the mesoscale rings, the upper part of the M1 mooring system significantly tilted (marked by colored lines on the top of Fig. 2), which resulted in missing data for both ADCPs and temperature profiles in the upper 500 m. Based on the 4-yr ADCPs and temperature chain collected by mooring M1, we identified three STEs with certainty in March 2016, May 2017, and July–August 2018. The corresponding migration of the STEs shows strong currents with reversed directions below the thermocline (Figs. 2a,b). In the following, we described detailed features of a warm-core STE (W7) and the dual-core STE (D1). The details of the other warm-core STE (W8) captured by M1 can be found in Table 2 and Fig. S8.

c. A warm-core STE in March 2016

In March 2016, a warm-core STE (W7) was captured by M1. Similar to the warm-core STE captured by KESS moorings, the observed velocity displays distinct maxima as the STE crosses the mooring (Fig. 8a). The V_{max} value of the STE W7 is 0.55 m s^{-1}, which is similar to that observed by the KESS moorings. The meridional velocity continued southward during the period of W7 (Fig. 8b), suggesting that it was the right-hand side of the STE that passed the mooring due south. Hence, we deduce that the crossing path is a chord rather than a diametrical axis of the circular STE.

The mooring system was pushed down by strong currents of this STE, with ADCPs and CTDs falling down almost 400 m (Fig. 8c). Referring to the T_e and H values derived from the current data, the positions of the two CTDs relative to the STE center during the STE passage can be roughly determined (gray shading in Fig. 8c). The maximum T_a and S_a during the STE passage reached +0.82°C and 0.13 psu, respectively, at 26.9σ_0 (Fig. 8d). These anomalous values are lower than those of the warm-core STE observed by KESS. This difference may be attributed to the chord path of M1 during the W7 crossing, while the path of K5 was likely along the STE diametrical axis. More details on mapping the possible paths of STE passages across moorings are given in section 4.

d. A dual-core STE in May 2017

As described in section 2, only the upward-looking ADCP on M1 at 400-m depth was available between April 2016 and May 2018, which, under normal conditions, cannot capture the STEs that are generally located below 400 m. However, the M1 mooring system experienced an extremely large knock-down event between 25 April and 25 May 2017. In particular, the ADCP descended from 400 to 1000 m (Figs. 9a,b), while two SBE 37-SM CTDs descended from 100 to 800 m and from 400 to 1100 m, respectively (Fig. 9c). A careful examination of the SSH field indicates that neither the surface-intensified eddy nor the KE jet crossed or came close to M1 (Fig. S9). We thus conclude that the strong currents associated with an STE during this period pushed the ADCPs and CTDs of the M1 mooring system to fluctuate over a depth range of 700 m. The dynamics of M1 was assessed using Mooring Design and Dynamics (MDD) software (Dewey 1999) and validated by comparing the modeled deepening of the mooring to the pressure sensor records of CTD probes. Based on the real configuration of the mooring M1 and the velocity time series recorded by ADCPs and current meters, the entire process of this knock-down event was simulated successfully (Fig. 10). The maximum modeled deepening reached ~400 m, which confirmed that subsurface velocities associated with the STE could cause the great vertical displacement of M1 (Fig. 10a). The ADCP data reveal an eddy-like flow pattern (caused by

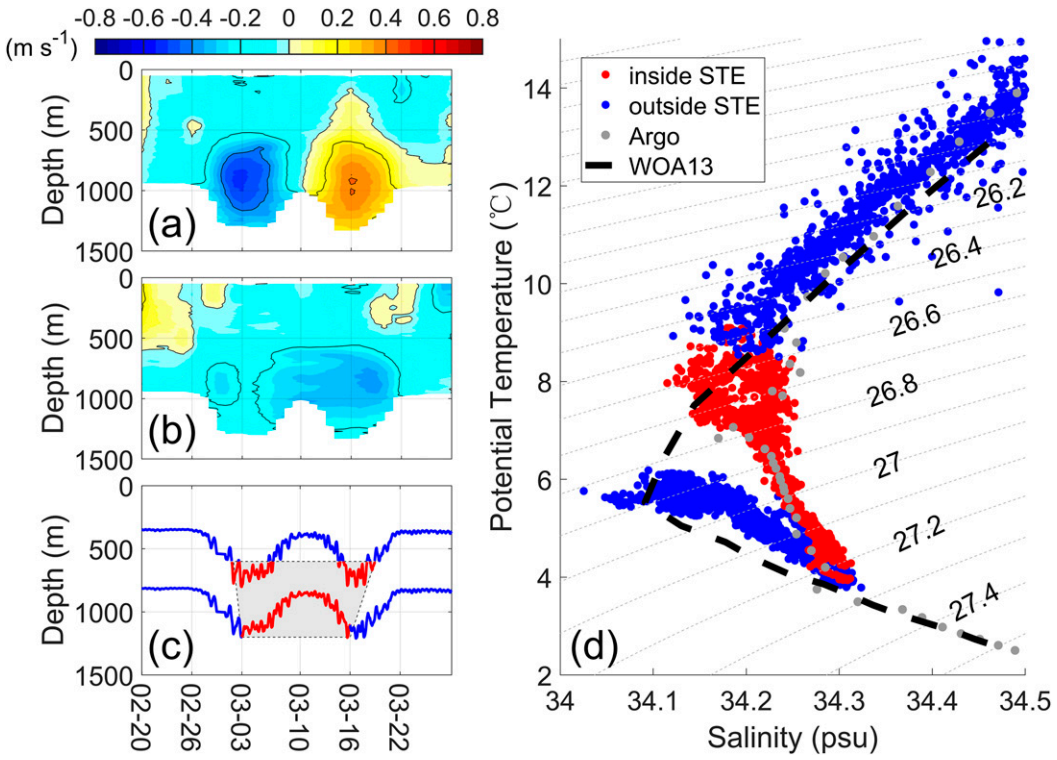

FIG. 8. Depth–time plots of (a) zonal velocity U and (b) meridional velocity V measured by ADCPs in March 2016. The contour interval is 0.2 m s^{-1}. (c) Depth of two CTDs as a function of time. CTDs in (out of) the rectangular gray box are regarded as being inside (outside) of the STE (W7) shown with red (blue) lines. (d) θ–S diagrams derived from the two CTDs. The red (blue) dots are θ/S values inside (outside) of the STE (W7). The black dashed line and the gray dots are derived from the *WOA13* climatology in March and nearby Argo floats (ID: 2902453), respectively.

STE passage) between 500 and 1000 m, with a V_{max} value of ~0.64 m s^{-1} and current directions reversing twice (Figs. 9a,b). The possible migration direction of this STE (i.e., D1) was northward according to the flow pattern. The northward migration of STE D1 is also confirmed by the trajectory of a nearby Argo float (Fig. 11a).

The most striking feature of the STE D1 is that it has two subsurface cores, with the upper cold/fresh core between 26.0σ_0 and 26.4σ_0 and the lower warm/salty core between 26.5σ_0 and 27.1σ_0 (Fig. 9d). The upper cold core is relatively thinner, with a thickness of ~100 m, but its T_a/S_a is large and reached −1.31°C/−0.31 psu at 26.2σ_0. In contrast, the lower warm core is much thicker (at least 500 m) but with a weaker T_a/S_a of +1.18°C/+0.19 psu at 27.0σ_0. This newly discovered dual-core STE is different from the previously reported double-core vortices (also called double-thermostad eddies), most of which being surface-intensified eddies containing a subsurface lens (Itoh and Yasuda 2010; Itoh et al. 2011; Meunier et al. 2018; Belkin et al. 2020).

To further demonstrate the robustness of the moored observations, the data from all Argo floats in the vicinity of M1 during that period are here analyzed. Fortunately, an Argo float (ID: 2903181) observed similar anomalous T/S profiles for two months (starting on 19 April) while this float was trapped inside STE D1 (Figs. 11a and 12). Temperature and salinity were sampled every 5 days by the float, and 11 anomalous profiles were eventually obtained by this Argo float inside the STE. The dual-core structure of this STE persisted during that period (Fig. 12). The shape of the θ/S distribution superimposed on the θ–S curves is identical to our observations from the mooring data (Fig. 9d). Based on all available Argo floats from 2004 to 2018 in the KE region (including 74041 vertical profiles), we obtained 22 profiles that captured dual-core STEs from five floats (Fig. 11b). In addition to the dual-core STE D1 in 2017 mentioned above and another STE found by a float (ID: 2900668) in 2007, three floats (ID: 2900142, 2900146, and 2900149) deployed by the KESS project might have captured the same dual-core STE successively between 2004 and 2005. To the best of our knowledge, this is the first report of this type of special dual-core STE in the KE region.

4. Radius and velocity structure of STEs

Following the method described in section 2e, the $\mathbf{V}_{STE}$ time series at the depth of V_{max} was selected during T_e, and the possible mooring path for each STE (in Table 2) was determined, as shown in Fig. 13. Here, we only focus on the movements within the interior eddy core ($<R$) and intercept $\mathbf{V}_{STE}$ values from two maxima, which indicated the moorings' first touch with and final departure from the STE. Except for three

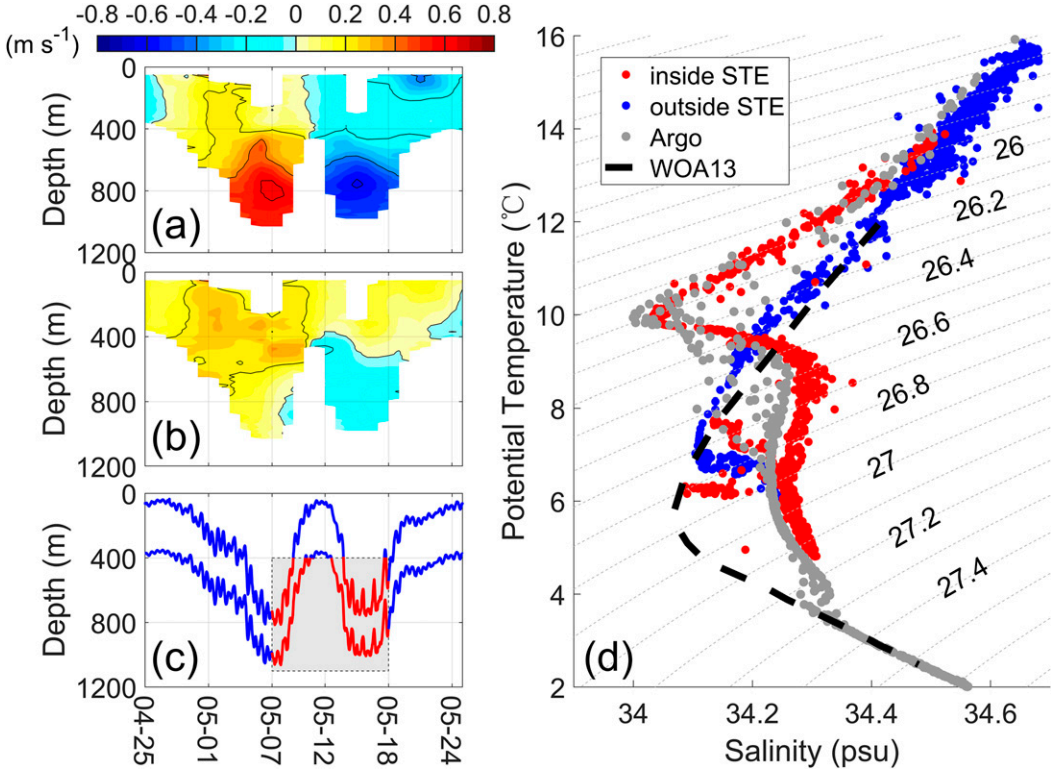

FIG. 9. As in Fig. 8, but for the dual-core STE (D1) from M1 in May 2017. The gray dots in (d) are θ/S measurements from an Argo float (ID: 2903181) during the STE passage.

warm-core STEs events for which the position of the mooring relative to the passing STE is unknown, there is a good consistency between the mooring path and the direction of $\mathbf{V}_b$, supporting the hypothesis that translation of STEs is primarily caused by the background flow advection. In most cases, the negative meridional component of $\mathbf{V}_b$ advected STEs southward, and the mooring would enter at their southern part and leave at their northern part.

Next, we estimated the radius of STEs using Eq. (3), and the results are listed in Table 2. As can be seen from the outlines of STEs in Figs. 4 and 6 and Figs. S1–S7, the warm-core STEs have a greater radius, with maximum R reaching 66.9 ± 26.6 km, while the maximum R of cold-core STEs is only 26.5 ± 11.8 km. It should be noted that because the background velocity profiles are not available for the dual-core STE in M1 due to missing ADCP data below 400 m, we use the mean drifting speed (0.08 m s^{-1}) of the nearby Argo float (ID: 2903181) as $\mathbf{V}_b$ instead. The parking depth of the Argo float is 1000 m so that $\mathbf{V}_b$ is somewhat weaker than the real background flow, which may lead to underestimation of the dual-core STE radius. Lilly and Rhines (2002) proposed a radius estimation method for SCVs using current meters from a mooring in the Labrador Sea. The major difference is that they used half the distance as the "apparent radius" given by background velocity times the SCV duration. If the mooring does not pass through the eddy core, this apparent radius will be less than the "real radius." Our method provides a direct estimation of the real radius no matter how eddies passed through the mooring, although there remained uncertainty due to the lack of real STE translation velocity and/or a real eddy model.

We further compared the STE radius with the internal Rossby deformation radius in this region. According to Dewar and Meng (1995), the radius of an STE can be estimated by the internal Rossby deformation radius, denoted by R_d:

$$R_d = \frac{N_0 H_0}{f}, \tag{4}$$

where N_0 is the background buoyancy frequency at the STE depth (approximately 0.005 s^{-1}), H_0 is the typical thickness of STEs (200 m for cold-core STEs and 600 m for warm-core STEs), and f is the local Coriolis parameter. The estimated R_d ranges from 13 to 38 km, which is generally within the magnitude scope of the above-calculated R.

The eddy Rossby number and Burger number of each STE (Table 2) are defined as follows:

$$\mathrm{Ro} = \frac{|\zeta|}{f}, \quad \mathrm{Bu} = \left(\frac{N_0 H}{fR}\right)^2, \tag{5}$$

where ζ is the vertical relative vorticity $[=(1/r)\partial(rV_{\mathrm{STE}})/\partial r]$ in cylindrical polar coordinates. Ro has an averaged value of ~0.5, which means that the centrifugal force plays an important role in the momentum balance. The values of Bu range from 0.25 to 8.07, with a median value of 0.97. Generally, most of the Bu values fall within the range of a theoretically stable

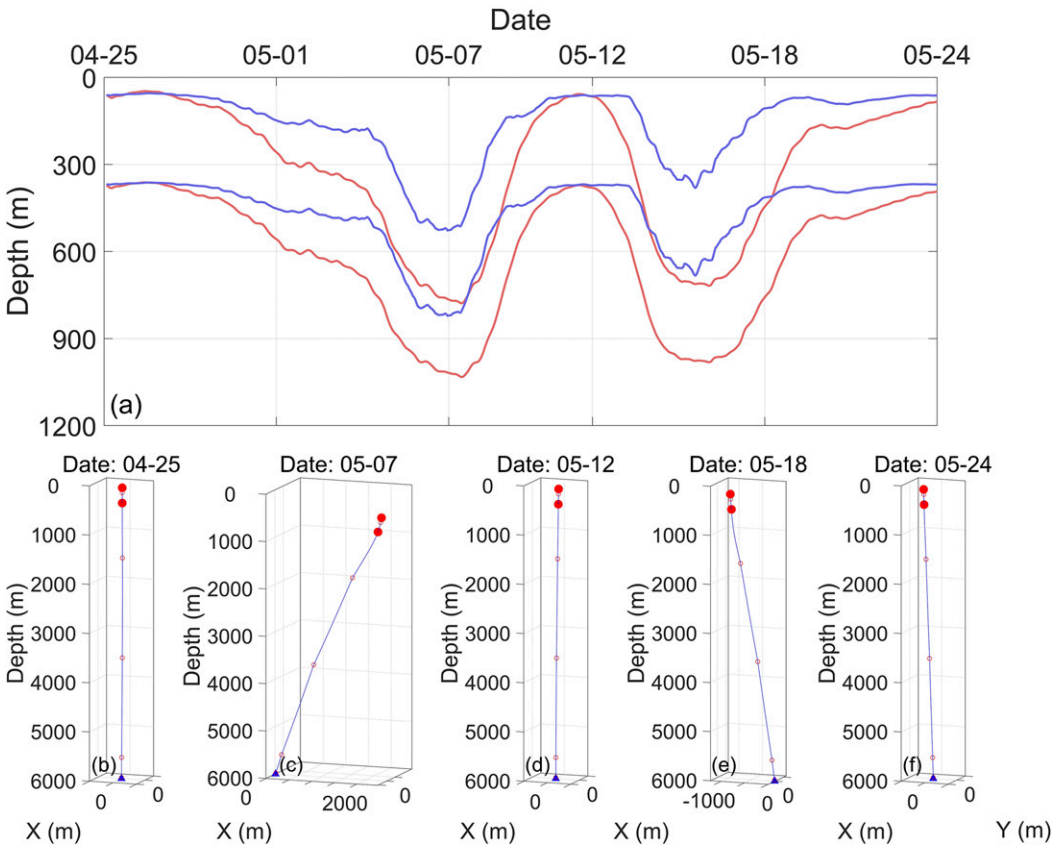

FIG. 10. (top) Depth–time plot of the depth data (read lines) recorded by two CTDs mounted on mooring M1 and the modeled depth by MDD software (blue lines). (bottom) The stable positions of mooring M1 at five moments of STE passage. Two solid red dots denote two CTDs on the mooring.

condition (0.05–1) for sustaining an STE (McWilliams 1985), which has been verified in sufficient observations for different types of SCVs in other areas. For instance, in the eastern North Pacific Ocean (Bower et al. 2013; Pelland et al. 2013; Steinberg et al. 2019), North Atlantic Ocean (Pietri and Karstensen 2018) and Mediterranean Sea (Testor and Gascard 2006; Bosse et al. 2016), all these SCVs have in common Ro/Bu values from $O(0.1)$ to $O(1)$ even though they are distributed at

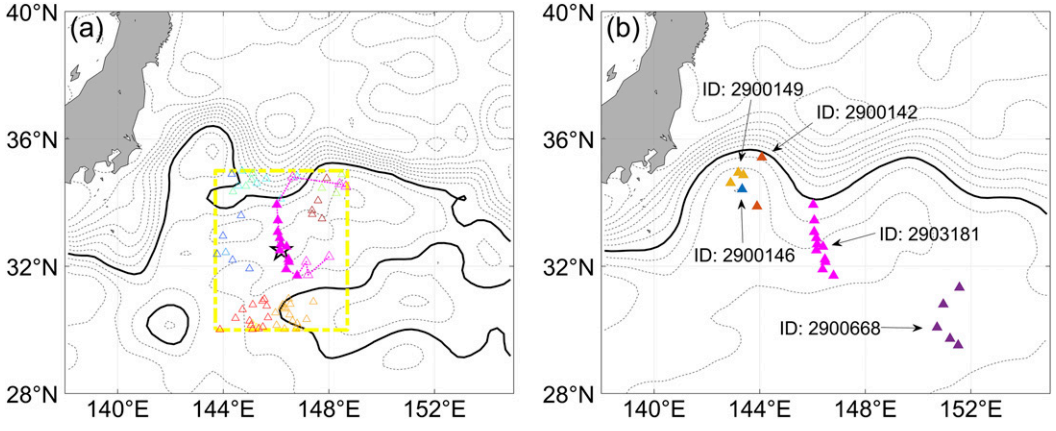

FIG. 11. (a) Locations of all Argo floats (triangles) in the yellow rectangle (5° × 5°) between April and June 2017. The solid triangles denote the profiles within the dual-core STE derived from the Argo float (ID: 2903181). The gray dashed lines and black lines are the long-term mean SSH field and the 120-cm contour averaged within this period, respectively. (b) Locations of Argo floats (triangles) that succeeded in capturing the dual-core STE between 2004 and 2018. The gray dashed lines and black lines denote the mean SSH field and the 120 cm contour, respectively, between 2004 and 2018.

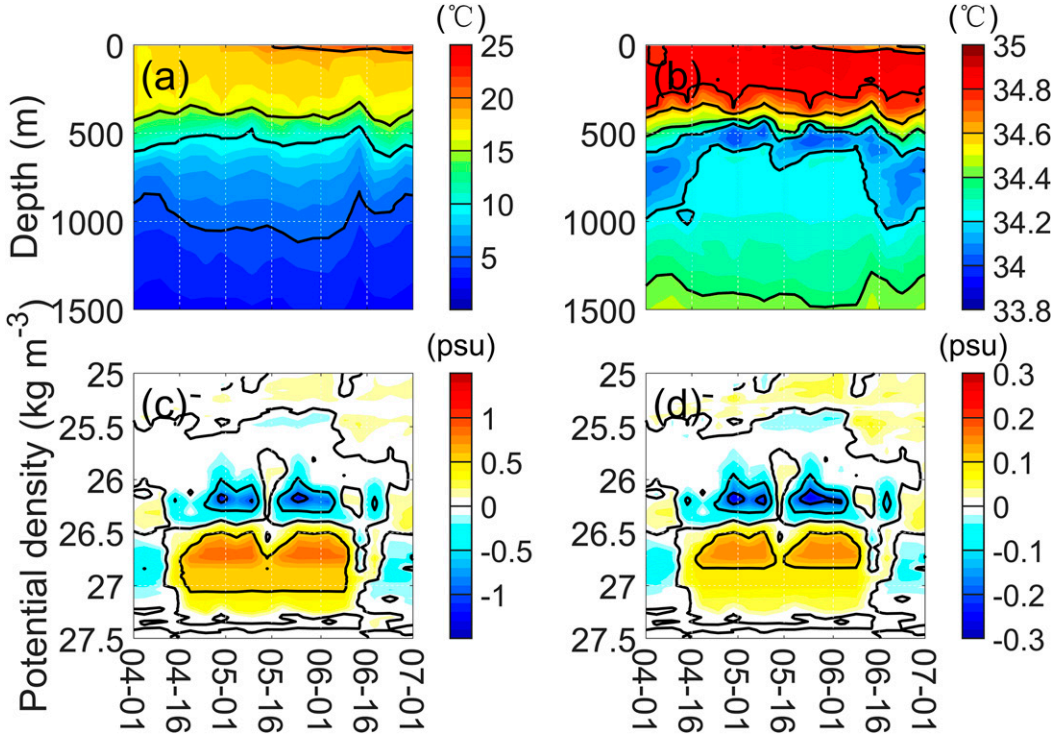

FIG. 12. Depth–time plot of (a) T, (b) S, (c) T_a, and (d) S_a on sigma levels from T/S measurements by an Argo float (ID: 2903181).

various depths with various sizes and water mass properties. The above results demonstrate that all three types of the observed STEs in the KE region are typical SCVs, supporting the previous argument for the water mass properties and dynamic characteristics of Kiddies based on Argo measurements (Zhang et al. 2015; Li et al. 2017).

5. Discussion on the possible origin and erosion of STEs

a. Possible origin regions

Typically, the STEs observed here have low-PV cores compared to the background PV, although some SCVs with high PV (positive ζ) have been found recently (Marez et al. 2020; Zhang et al. 2021). Based on the impermeability theorem (Haynes and McIntyre 1987), the net transport of PV could hardly cross the isopycnic surfaces in the absence of diapycnal mixing. Hence, the low PV of an STE must be created between two given isopycnic surfaces through nonconservative or diabatic processes. This extreme PV anomaly of the STE is most likely generated at the boundaries rather than in the interior ocean. At the sea surface, deep convection in winter provides a PV destruction source or PV sink by reducing stratification, which is very common in the Mediterranean (Testor and Gascard 2006; Bosse et al. 2016). Thomas (2008) used a high-resolution numerical simulation to examine another mechanism for the destruction of PV by wind-driven friction in the frontal outcropping isopycnals. Below the surface, the PV source caused by the flow–topography interaction may play an essential role in the generation of STEs (Molemaker et al. 2015; Gula et al. 2019; Srinivasan et al. 2019; Zhang et al. 2020). The Cuddies, for instance, have been demonstrated to be formed by the interaction of the California Undercurrent with complex topography (Pelland et al. 2013; Molemaker et al. 2015).

After generations, the STEs usually move along isopycnals by conserving their water mass properties to a large extent; thus, their origins could be inferred from θ or S distributions on specific isopycnals (Bower et al. 2013; Zhang et al. 2015). Here, we did not use salinity as a tracer because the temperatures within observed STEs were colder than 10°C. This condition suggested that the STEs may originate from beta oceans (Carmack 2007), where the density is dominated by salinity and the temperature is relatively conservative. As mentioned above, the cold-core STE captured by KESS moorings and the upper part of the dual-core STE captured by M1 have T_a minima at approximately $26.2\sigma_0$, while the warm-core STE and the lower part of the dual-core STE captured by M1 have T_a maxima at approximately $26.9\sigma_0$. Figure 14a shows that the cold-core STEs may originate from the SAF region, which agrees with the conclusion of Zhang et al. (2015) and Li et al. (2017). Therefore, these cold-core STEs can be generated through subduction processes in the wintertime mixed layer as proposed in previous studies (Oka et al. 2009; Li et al. 2017). The origin of warm-core STEs, however, is still not clear at this stage. One possible origin of the warm-core STEs can be traced back upstream along the Kuroshio to the south of Japan (Fig. 14b). Typically, the Kuroshio crosses over the Izu Ridge before flowing into the KE region. Similar to the bottom boundary layer processes in the Gulf Stream, submesoscale vortices and

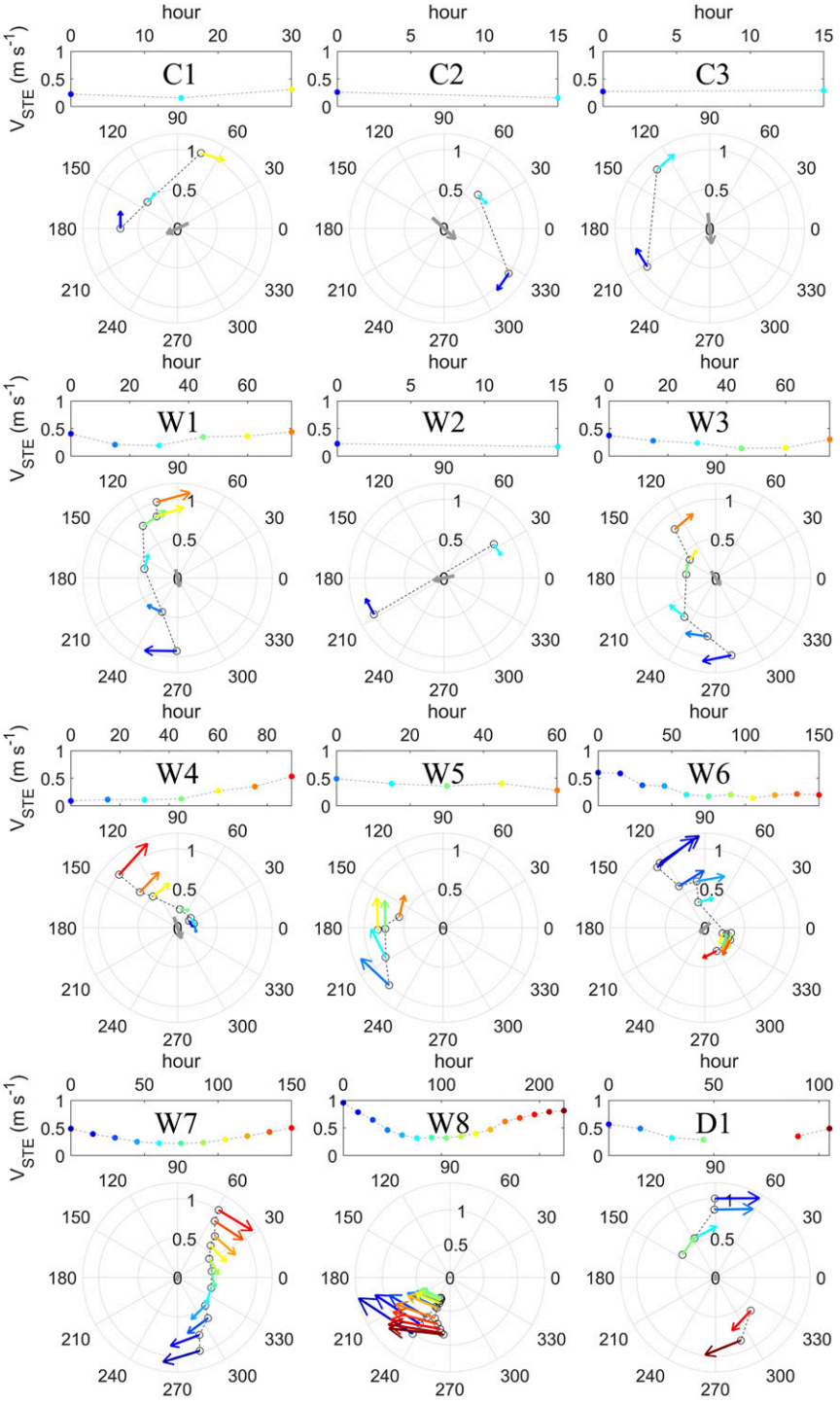

FIG. 13. Azimuthal velocity of each STE listed in Table 2 and the possible path (black dashed line in the cycle). The origin in the cycle denotes the center of each STE and the number 0 (90) on the right (top) side of the cycle represents the east (north) direction. Dots in the cycle are mooring positions relative to the STE center with colored vector corresponding to the swirl velocity of STE ($\mathbf{V}_{STE}$) at different time. The gray vector in the origin of each cycle is $\mathbf{V}_b$.

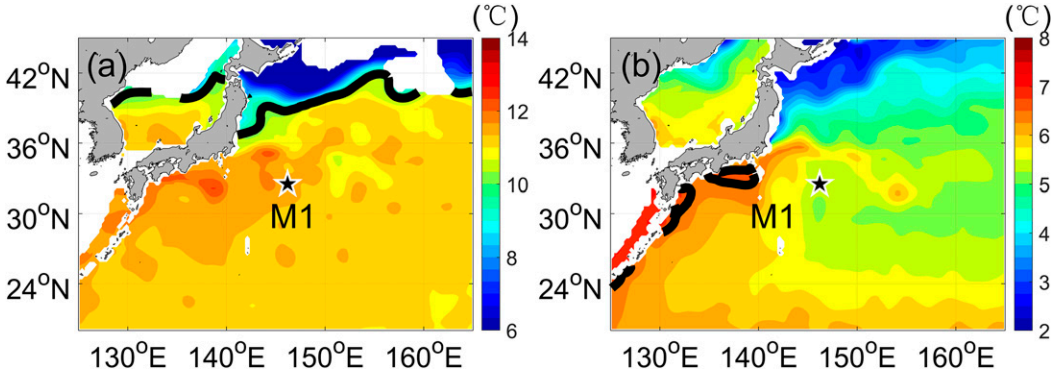

FIG. 14. Distributions of θ on the (a) $26.2\sigma_0$ and (b) $26.9\sigma_0$ surfaces. The black star indicates the location of the M1 mooring. The black lines in (a) and (b) are contours of 10.0° and 6.5°C on the respective isopycnals.

filaments could be generated by velocity shear associated with the ridge or continental shelf and gradually organize into STEs through horizontal merger or vertical alignment (Srinivasan et al. 2019). Based on a submesoscale-resolving simulation, Gula et al. (2019) revealed that the Gulf Stream interacts with the Charleston Bump to form STEs in the wake of the Bump. Armi (1978) studied vorticity formation by weaker deep western boundary currents in a weakly stratified environment and showed that this mechanism could generate STEs with warm and salty water. The destruction of PV caused by the lateral/bottom friction is generally not as severe as that caused by convection, which can reduce the water stratification to almost zero (Bosse et al. 2016).

For the dual-core STE, as shown in Fig. 14, the θ contours of the two centers are disjointed in the northwestern Pacific, implying that it is impossible to generate this type of STE with two distinct cores at the very beginning. It should be noted that some Meddies do have two cores in the vertical direction, but they share similar warm and salty water properties both from the Mediterranean outflow. While this particular θ/S distribution of a dual-core STE with two different water properties could not be found in any single origination in the KE region. Griffiths and Hopfinger (1987) proposed the possibility that the anticyclonic vortices of different densities have a tendency to align in a stratified rotating fluid. In other words, a cold-core STE may have come above a warm-core STE with the same rotation direction and have subsequently formed a single vortex. However, due to the small scales of STEs, we cannot assess the probabilities of such coalescence base on limited observations of STEs. Very high-resolution model simulations may be needed to address this issue.

b. *Possible erosion process*

The STEs conserve the interior water properties during their migration by virtue of PV barrier to restrict the exchange and diffusion with surrounding waters for a long time. Understanding the process of STE erosion may be beneficial for quantitatively estimating the salt, heat, nutrient, and oxygen transport along paths far from their origins. Some studies have argued that the near-inertial waves could be trapped by the mesoscale or submesoscale eddy and near-inertial energy may be focused to increase the dissipation levels at the bottom of an eddy (Lueck and Osborn 1986; Fer et al. 2018; Zhang et al. 2018; Fernández-Castro et al. 2020; Lelong et al. 2020). A recent study based on moorings revealed that shear instability was greatly enhanced by an STE in the western equatorial Pacific, which led to a significant enhancement in diapycnal mixing (Zhang et al. 2019). Based on rough energetics analysis, Zhang et al. (2019) further proposed that the turbulent dissipation caused by the STE-induced shear instability may be an important erosion mechanism for STEs.

In Fig. 15, we illustrate the velocity shear variance ($S^2 = |\partial u/\partial z|^2 + |\partial v/\partial z|^2$), where u and v are the zonal and meridional velocities, respectively, during the warm-core STE at M1. In the upper periphery of the STE, the S^2 is enhanced and its maxima reaches $10^{-4}\,\mathrm{m^{-1}\,s^{-1}}$. Although no moored data are available to derive the stratification, we estimate the Richardson number ($\mathrm{Ri} = N^2/S^2$) based on one N^2 profile derived from an Argo float (ID: 2902453), which shares the same θ/S properties in the STE (Fig. 8d). The result shows that upon approaching the STE, Ri begins to decrease and in some instances decreases below 0.25, suggesting the potential occurrence of shear instability (Fig. 15d). Examining the shear spectrum revealed that the shear variance is primarily dominated by the subinertial and near-inertial components (figure not shown). To investigate whether the subinertial shear associated with the STE alone can induce shear instability, as found by Zhang et al. (2019) in the western equatorial Pacific, we then calculated the subinertial (near-inertial) shear using a fourth-order Butterworth low-pass (bandpass) filter with a cutoff frequency of $0.75f$ ($0.75f$–$1.25f$), where f is the local inertial frequency. The results show that if Ri is calculated using only the subinertial or near-inertial shear, it is much larger than 0.25. The above findings suggest that the strong subinertial shear of the STE may favor internal wave breaking to induce shear instability, which can indirectly enhance the diapycnal mixing. This mixing mechanism may provide a possible route for erosion of STEs.

6. Summary

In this study, the kinematic and dynamic characteristics of the STEs in the KE, which were named Kiddies in the previous Argo-based study (Li et al. 2017), are investigated for the first

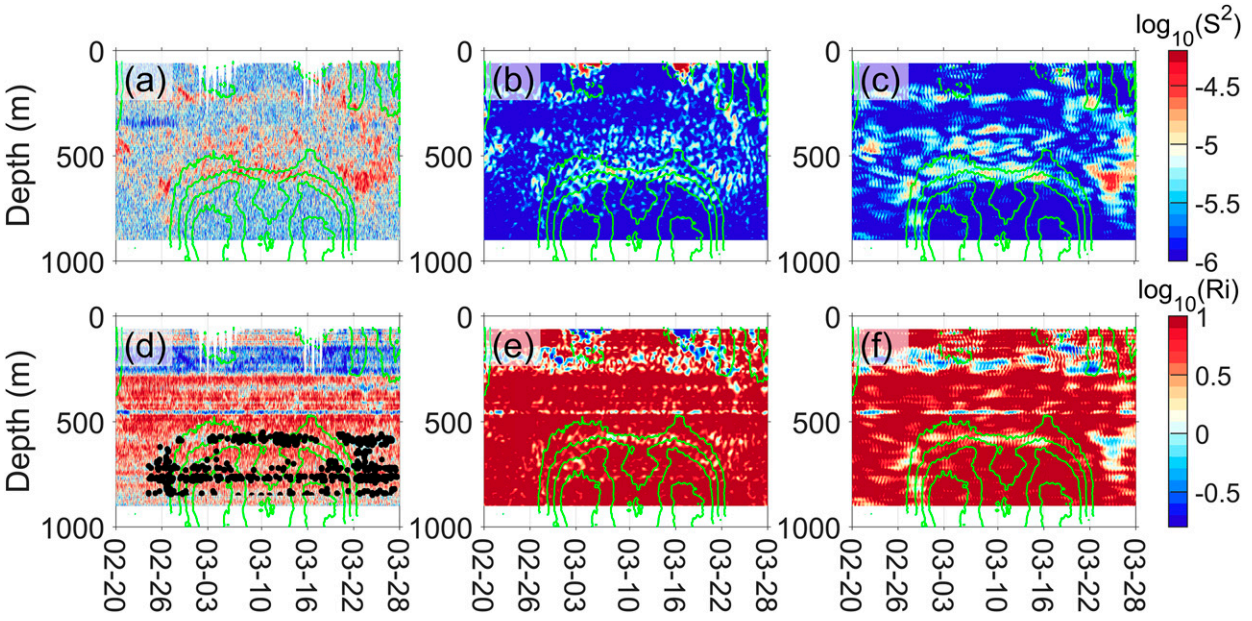

FIG. 15. Depth–time plots of (a) original, (b) subinertial, and (c) near-inertial S^2 during the warm-core STE crossing of M1. (d)–(f) As in (a)–(c), but for the Ri value. The black dots in (d) are Ri values less than 0.25. The green contours are the absolute velocity larger than 0.2 m s^{-1} with an interval of 0.1 m s^{-1}. All values are shown on a logarithmic scale.

time using concurrent moored T/S and velocity observations. The cold-core STEs generally have smaller volumes, lower swirl speeds and stronger θ/S and PV anomalies compared with the warm-core STEs. The cold-core STEs may originate from the subarctic front by subduction and/or vertical motions associated with frontal meanders into the subsurface, while the warm-core STEs could be generated through friction with the topography in the upstream region of Kuroshio south of Japan. A dual-core STE, with the two cores containing contrasting θ/S properties, was detected in May 2017 by the M1 mooring. The upper (lower) cores were similar to the cold-core (warm-core) STEs, with a thickness of approximately 190 m (400 m) and T_a/S_a reaching −1.31°C/−0.31 psu (1.18°C/0.19 psu). Nevertheless, only one maximum swirl speed was found in the velocity structure, implying that the dual-core STE rotates as a whole vortex rather than two vortices. Based on current observations from the moorings, a diagnostic method is proposed to estimate the STE radii and its possible paths when crossing the mooring. The results show that the radius estimations based on observed currents are to some extent larger than those calculated by θ/S profiles, with the maximum R reaching ~60 km. According to their thermohaline features and the high Rossby number (~0.5) and $O(1)$ Burger number, these STEs can be considered as submesoscale coherent vortices. The low Richardson number on the upper periphery of STEs suggests that the shear instability could induce turbulent mixing, which may be an erosion route for the STEs. The detailed generation and erosion mechanisms of the STEs in the KE region needs to be further studied in the future based on more high-resolution observations and model simulations.

Acknowledgments. The authors would thank two reviewers for providing insight comments on this paper. This research is funded by the National Natural Science Foundation of China (42076009, 41806008, 41706005, and 42076004), the National Key Research and Development Program of China (2016YFC1402606), and the Qingdao Pilot National Laboratory for Marine Science and Technology (2017ASTCPES05 and 2017ASKJ01). Z. C. is partially supported by the 'Taishan' Talents program and other related funds (201762013).

REFERENCES

Argo, 2000: Argo float data and metadata from Global Data Assembly Centre (Argo GDAC). SEANOE, accessed 9 March 2020, https://doi.org/10.17882/42182.

Armi, L., 1978: Some evidence for boundary mixing in the deep ocean. *J. Geophys. Res.*, **83**, 1971–1979, https://doi.org/10.1029/JC083iC04p01971.

——, D. Hebert, N. Oakey, J. F. Price, P. L. Richardson, H. T. Rossby, and B. Ruddick, 1989: Two years in the life of a Mediterranean salt lens. *J. Phys. Oceanogr.*, **19**, 354–370, https://doi.org/10.1175/1520-0485(1989)019<0354:TYITLO>2.0.CO;2.

Baird, M. E., and K. R. Ridgway, 2012: The southward transport of sub-mesoscale lenses of Bass Strait Water in the centre of anticyclonic mesoscale eddies. *Geophys. Res. Lett.*, **39**, L02603, https://doi.org/10.1029/2011GL050643.

Belkin, I., A. Foppert, T. Rossby, S. Fontana, and C. Kincaid, 2020: A double-thermostad warm-core ring of the Gulf Stream. *J. Phys. Oceanogr.*, **50**, 489–507, https://doi.org/10.1175/JPO-D-18-0275.1.

Bosse, A., P. Testor, L. Mortier, L. Prieur, V. Taillandier, F. d'Ortenzio, and L. Coppola, 2015: Spreading of Levantine Intermediate Waters by submesoscale coherent vortices in the northwestern Mediterranean Sea as observed with gliders. *J. Geophys. Res. Oceans*, **120**, 1599–1622, https://doi.org/10.1002/2014JC010263.

——, and Coauthors, 2016: Scales and dynamics of submesoscale coherent vortices formed by deep convection in the northwestern

Mediterranean Sea. *J. Geophys. Res. Oceans*, **121**, 7716–7742, https://doi.org/10.1002/2016JC012144.

——, I. Fer, J. M. Lilly, and H. Søiland, 2019: Dynamical controls on the longevity of a non-linear vortex: The case of the Lofoten Basin eddy. *Sci. Rep.*, **9**, 13448, https://doi.org/10.1038/s41598-019-49599-8.

Bower, A. S., R. M. Hendry, D. E. Amrhein, and J. M. Lilly, 2013: Direct observations of formation and propagation of subpolar eddies into the subtropical North Atlantic. *Deep-Sea Res. II*, **85**, 15–41, https://doi.org/10.1016/j.dsr2.2012.07.029.

Carmack, E. C., 2007: The alpha/beta ocean distinction: A perspective on freshwater fluxes, convection, nutrients and productivity in high-latitude seas. *Deep-Sea Res. II*, **54**, 2578–2598, https://doi.org/10.1016/j.dsr2.2007.08.018.

De Jong, M., A. Bower, and H. H. Furey, 2014: Two years of observations of warm-core anticyclones in the Labrador Sea and their seasonal cycle in heat and salt stratification. *J. Phys. Oceanogr.*, **44**, 427–444, https://doi.org/10.1175/JPO-D-13-070.1.

Dewar, W. K., and H. Meng, 1995: The propagation of submesoscale coherent vortices. *J. Phys. Oceanogr.*, **25**, 1745–1770, https://doi.org/10.1175/1520-0485(1995)025<1745:TPOSCV>2.0.CO;2.

Dewey, R. K., 1999: Mooring Design & Dynamics—A Matlab package for designing and analyzing oceanographic moorings. *Mar. Models*, **1**, 103–157, https://doi.org/10.1016/S1369-9350(00)00002-X.

Donohue, K., D. R. Watts, K. Tracey, M. Wimbush, and S. Jayne, 2008: Program studies the Kuroshio extension. *Eos, Trans. Amer. Geophys. Union*, **89**, 161–162, https://doi.org/10.1029/2008EO170002.

Dugan, J. P., R. R. Mied, P. C. Mignerey, and A. F. Schuetz, 1982: Compact, intrathermocline eddies in the Sargasso Sea. *J. Geophys. Res.*, **87**, 385–393, https://doi.org/10.1029/JC087iC01p00385.

Ertel, H., 1942: Ein neuer hydrodynamischer Wirbelsatz. *Meteor. Z.*, **59**, 277–281.

Fer, I., A. Bosse, B. Ferron, and P. Bouruet-Aubertot, 2018: The dissipation of kinetic energy in the Lofoten Basin eddy. *J. Phys. Oceanogr.*, **48**, 1299–1316, https://doi.org/10.1175/JPO-D-17-0244.1.

Fernández-Castro, B., D. G. Evans, E. Frajka-Williams, C. Vic, and A. C. Naveira-Garabato, 2020: Breaking of internal waves and turbulent dissipation in an anticyclonic mode water eddy. *J. Phys. Oceanogr.*, **50**, 1893–1914, https://doi.org/10.1175/JPO-D-19-0168.1.

Garfield, N., C. A. Collins, R. G. Paquette, and E. Carter, 1999: Lagrangian exploration of the California Undercurrent, 1992–95. *J. Phys. Oceanogr.*, **29**, 560–583, https://doi.org/10.1175/1520-0485(1999)029<0560:LEOTCU>2.0.CO;2.

Griffiths, R., and E. Hopfinger, 1987: Coalescing of geostrophic vortices. *J. Fluid Mech.*, **178**, 73–97, https://doi.org/10.1017/S0022112087001125.

Gula, J., T. M. Blacic, and R. E. Todd, 2019: Submesoscale coherent vortices in the Gulf Stream. *Geophys. Res. Lett.*, **46**, 2704–2714, https://doi.org/10.1029/2019GL081919.

Haynes, P. H., and M. E. McIntyre, 1987: On the evolution of vorticity and potential vorticity in the presence of diabetic heating and frictional or other forces. *J. Atmos. Sci.*, **44**, 828–841, https://doi.org/10.1175/1520-0469(1987)044<0828:OTEOVA>2.0.CO;2.

Hebert, D., N. Oakey, and B. Ruddick, 1990: Evolution of a Mediterranean salt lens: Scalar properties. *J. Phys. Oceanogr.*, **20**, 1468–1483, https://doi.org/10.1175/1520-0485(1990)020<1468:EOAMSL>2.0.CO;2.

Itoh, S., and I. Yasuda, 2010: Water mass structure of warm and cold anticyclonic eddies in the western boundary region of the subarctic North Pacific. *J. Phys. Oceanogr.*, **40**, 2624–2642, https://doi.org/10.1175/2010JPO4475.1.

——, Y. Shimizu, S. I. Ito, and I. Yasuda, 2011: Evolution and decay of a warm-core ring within the western subarctic gyre of the North Pacific, as observed by profiling floats. *J. Phys. Oceanogr.*, **67**, 281–293, https://doi.org/10.1007/s10872-011-0027-2.

Johnson, G. C., and K. E. McTaggart, 2010: Equatorial Pacific 13°C water eddies in the eastern subtropical South Pacific Ocean. *J. Phys. Oceanogr.*, **40**, 226–236, https://doi.org/10.1175/2009JPO4287.1.

Kostianoy, A. G., and I. M. Belkin, 1989: A survey of observations on intrathermocline eddies in the world ocean. *Mesoscale/Synoptic Coherent Structures in Geophysical Turbulence*, J. C. J. Nihoul and B. M. Jamart, Eds., Elsevier Oceanography Series, Vol. 50, Elsevier, 821–841, https://doi.org/10.1016/S0422-9894(08)70223-X.

L'Hégaret, P., and Coauthors, 2014: Evidence of Mediterranean water dipole collision in the Gulf of Cadiz. *J. Geophys. Res. Oceans*, **119**, 5337–5359, https://doi.org/10.1002/2014JC009972.

Lelong, M. P., Y. Cuypers, and P. Bouruet-Aubertot, 2020: Near-inertial energy propagation inside a Mediterranean anticyclonic eddy. *J. Phys. Oceanogr.*, **50**, 2271–2288, https://doi.org/10.1175/JPO-D-19-0211.1.

Li, C., Z. Zhang, W. Zhao, and J. Tian, 2017: A statistical study on the subthermocline submesoscale eddies in the northwestern Pacific Ocean based on Argo data. *J. Geophys. Res. Oceans*, **122**, 3586–3598, https://doi.org/10.1002/2016JC012561.

Lilly, J. M., and P. B. Rhines, 2002: Coherent eddies in the Labrador Sea observed from a mooring. *J. Phys. Oceanogr.*, **32**, 585–598, https://doi.org/10.1175/1520-0485(2002)032<0585:CEITLS>2.0.CO;2.

Locarnini, R. A., and Coauthors, 2013: *Temperature*. Vol. 1, *World Ocean Atlas 2013*, NOAA Atlas NESDIS 73, 40 pp., http://data.nodc.noaa.gov/woa/WOA13/DOC/woa13_vol1.pdf.

Lueck, R., and T. Osborn, 1986: The dissipation of kinetic energy in a warm-core ring. *J. Geophys. Res.*, **91**, 803–818, https://doi.org/10.1029/JC091iC01p00803.

Ma, X., P. Chang, R. Saravanan, R. Montuoro, J. S. Hsieh, D. Wu, and Z. Jing, 2015: Distant influence of Kuroshio eddies on North Pacific weather patterns? *Sci. Rep.*, **5**, 17785, https://doi.org/10.1038/srep17785.

Marez, C. D., X. Carton, S. Corréard, P. L'Hégaret, and M. Morva, 2020: Observations of a deep submesoscale cyclonic vortex in the Arabian Sea. *Geophys. Res. Lett.*, **47**, e2020GL087881, https://doi.org/10.1029/2020GL087881..

Maximenko, N. A., and T. Yamagata, 1995: Submesoscale anomalies in the North Pacific subarctic front. *J. Geophys. Res.*, **100**, 18 459–18 469, https://doi.org/10.1029/95JC01565.

McDowell, S. E., and H. T. Rossby, 1978: Mediterranean water: An intense mesoscale eddy off the Bahamas. *Science*, **202**, 1085–1087, https://doi.org/10.1126/science.202.4372.1085.

McWilliams, J. C., 1985: Submesoscale, coherent vortices in the ocean. *Rev. Geophys.*, **23**, 165–182, https://doi.org/10.1029/RG023i002p00165.

——, 2016: Submesoscale currents in the ocean. *Proc. Roy. Soc.*, **472A**, 20160117, https://doi.org/10.1098/rspa.2016.0117.

Meunier, T., and Coauthors, 2018: Intrathermocline eddies embedded within an anticyclonic vortex ring. *Geophys. Res. Lett.*, **45**, 7624–7633, https://doi.org/10.1029/2018GL077527.

Mizuno, K., and W. B. White, 1983: Annual and interannual variability in the Kuroshio Current system. *J. Phys. Oceanogr.*, **13**,

1847–1867, https://doi.org/10.1175/1520-0485(1983)013<1847:AAIVIT>2.0.CO;2.

Molemaker, M. J., J. C. McWilliams, and W. K. Dewar, 2015: Submesoscale instability and generation of mesoscale anticyclones near a separation of the California Undercurrent. *J. Phys. Oceanogr.*, **45**, 613–629, https://doi.org/10.1175/JPO-D-13-0225.1.

Nakamura, H., T. Izumi, and T. Sampe, 2002: Interannual and decadal modulations recently observed in the Pacific storm track activity and East Asian winter monsoon. *J. Climate*, **15**, 1855–1874, https://doi.org/10.1175/1520-0442(2002)015<1855:IADMRO>2.0.CO;2.

Oka, E., K. Toyama, and T. Suga, 2009: Subduction of North Pacific central mode water associated with subsurface mesoscale eddy. *Geophys. Res. Lett.*, **36**, L08607, https://doi.org/10.1029/2009GL037540.

Pelland, N., C. C. Eriksen, and C. M. Lee, 2013: Subthermocline eddies over the Washington continental slope as observed by Seagliders, 2003–09. *J. Phys. Oceanogr.*, **43**, 2025–2053, https://doi.org/10.1175/JPO-D-12-086.1.

Pietri, A., and J. Karstensen, 2018: Dynamical characterization of a low oxygen submesoscale coherent vortex in the eastern North Atlantic Ocean. *J. Geophys. Res. Oceans*, **123**, 2049–2065, https://doi.org/10.1002/2017JC013177.

Qiu, B., and S. Chen, 2005: Variability of the Kuroshio extension jet, recirculation gyre, and mesoscale eddies on decadal time scales. *J. Phys. Oceanogr.*, **35**, 2090–2103, https://doi.org/10.1175/JPO2807.1.

Rainville, L., S. Jayne, N. Hogg, and S. Waterman, 2009: KESS data report –WHOI subsurface moorings. WHOI, 15 pp., http://mmmfire.whoi.edu/uskess/data/KESS%20Data%20Report%20%E2%80%93%20WHOI%20subsurface%20moorings.pdf.

Rossby, T., C. Flagg, P. Ortner, and C. Hu, 2011: A tale of two eddies: Diagnosing coherent eddies through acoustic remote sensing. *J. Geophys. Res.*, **116**, C12017, https://doi.org/10.1029/2011JC007307.

Shapiro, G. I., and S. L. Meschanov, 1991: Distribution and spreading of Red Sea Water and salt lens formation in the northwest Indian Ocean. *Deep-Sea Res. I*, **38**, 21–34, https://doi.org/10.1016/0198-0149(91)90052-H.

——, W. Zenk, S. L. Meschanov, and K. L. Schultz Tokos, 1995: Self-similarity of the meddy family in the eastern North Atlantic. *Oceanol. Acta*, **18**, 29–42.

Spall, M. A., 1995: Frontogenesis, subduction, and cross-front exchange at upper ocean fronts. *J. Geophys. Res.*, **100**, 2543–2557, https://doi.org/10.1029/94JC02860.

Srinivasan, K., J. C. McWilliams, M. J. Molemaker, and R. Barkan, 2019: Submesoscale vortical wakes in the lee of topography. *J. Phys. Oceanogr.*, **49**, 1949–1971, https://doi.org/10.1175/JPO-D-18-0042.1.

Steinberg, J. M., N. A. Pelland, and C. C. Eriksen, 2019: Observed evolution of a California Undercurrent Eddy. *J. Phys. Oceanogr.*, **49**, 649–674, https://doi.org/10.1175/JPO-D-18-0033.1.

Testor, P., and J. C. Gascard, 2003: Large-scale spreading of deep waters in the western Mediterranean Sea by submesoscale coherent eddies. *J. Phys. Oceanogr.*, **33**, 75–87, https://doi.org/10.1175/1520-0485(2003)033<0075:LSSODW>2.0.CO;2.

——, and ——, 2006: Post-convection spreading phase in the northwestern Mediterranean Sea. *Deep-Sea Res. I*, **53**, 869–893, https://doi.org/10.1016/j.dsr.2006.02.004.

Thomas, L. N., 2008: Formation of intrathermocline eddies at ocean fronts by wind-driven destruction of potential vorticity. *Dyn. Atmos. Oceans*, **45**, 252–273, https://doi.org/10.1016/j.dynatmoce.2008.02.002.

Thomsen, S., T. Kanzow, G. Krahmann, R. J. Greatbatch, M. Dengler, and G. Lavik, 2016: The formation of a subsurface anticyclonic eddy in the Peru-Chile Undercurrent and its impact on the near-coastal salinity, oxygen, and nutrient distributions. *J. Geophys. Res. Oceans*, **121**, 476–501, https://doi.org/10.1002/2015JC010878.

Timmermans, M. L., J. Toole, A. Proshutinsky, R. Krishfield, and A. Plueddemann, 2008: Eddies in the Canada basin, Arctic Ocean, observed from ice-tethered profilers. *J. Phys. Oceanogr.*, **38**, 133–145, https://doi.org/10.1175/2007JPO3782.1.

Yasuda, I., K. Okuda, and M. Hirai, 1992: Evolution of a Kuroshio warm-core ring—Variability of the hydrographic structure. *Deep-Sea Res. I*, **39**, S131–S161, https://doi.org/10.1016/S0198-0149(11)80009-9.

Yu, L.-S., A. Bosse, I. Fer, K. A. Orvik, E. M. Bruvik, I. Hessevik, and K. Kvalsund, 2017: The Lofoten Basin eddy: Three years of evolution as observed by Seagliders. *J. Geophys. Res. Oceans*, **122**, 6814–6834, https://doi.org/10.1002/2017JC012982.

Zhang, Z., P. Li, L. Xu, C. Li, W. Zhao, J. Tian, and T. Qu, 2015: Subthermocline eddies observed by rapid-sampling Argo floats in the subtropical northwestern Pacific Ocean in spring 2014. *Geophys. Res. Lett.*, **42**, 6438–6445, https://doi.org/10.1002/2015GL064601.

——, B. Qiu, J. Tian, W. Zhao, and X. Huang, 2018: Latitude-dependent finescale turbulent shear generations in the Pacific tropical-extratropical upper ocean. *Nat. Commun.*, **9**, 4086, https://doi.org/10.1038/s41467-018-06260-8.

——, Z. Liu, K. Richards, G. Shang, W. Zhao, J. Tian, and C. Zhou, 2019: Elevated diapycnal mixing by a subthermocline eddy in the western equatorial Pacific. *Geophys. Res. Lett.*, **46**, 2628–2636, https://doi.org/10.1029/2018GL081512.

——, Y. Zhang, B. Qiu, H. Sasaki, Z. Sun, X. Zhang, W. Zhao, and J. Tian, 2020: Spatiotemporal characteristics and generation mechanisms of submesoscale currents in the northeastern South China Sea revealed by numerical simulations. *J. Geophys. Res. Oceans*, **125**, e2019JC015404, https://doi.org/10.1029/2019JC015404.

——, X. Zhang, B. Qiu, W. Zhao, C. Zhou, X. Huang, and J. Tian, 2021: Submesoscale currents in the subtropical upper ocean observed by long-term high-resolution mooring arrays. *J. Phys. Oceanogr.*, **51**, 187–206, https://doi.org/10.1175/JPO-D-20-0100.1.

Zhao, M., and M. L. Timmermans, 2015: Vertical scales and dynamics of eddies in the Arctic Ocean's Canada basin. *J. Geophys. Res. Oceans*, **120**, 8195–8209, https://doi.org/10.1002/2015JC011251.

Zweng, M., and Coauthors, 2013: *Salinity*. Vol. 2, *World Ocean Atlas 2013*, NOAA Atlas NESDIS 74, 39 pp., http://data.nodc.noaa.gov/woa/WOA13/DOC/woa13_vol2.pdf.